Up-Regulation of Rho/ROCK Signaling in Sarcoma Cells Drives Invasion and Increased Generation of Protrusive Forces

Daniel Rösel,[1] Jan Brábek,[1] Ondřej Tolde,[1] Claudia T. Mierke,[3] Daniel P. Zitterbart,[3] Carina Raupach,[3] Kristýna Bicanová,[1] Philip Kollmannsberger,[3] Daniela Paňková,[1] Pavel Veselý,[2] Petr Folk,[1] and Ben Fabry[3]

[1]Department of Cell Biology, Faculty of Science, Charles University in Prague; [2]Institute of Molecular Genetics AS, Prague, Czech Republic; and [3]Biophysics Group, Department of Physics, University of Erlangen-Nuremberg, Erlangen, Germany

Abstract

Tumor cell invasion is the most critical step of metastasis. Determination of the mode of invasion within the particular tumor is critical for effective cancer treatment. Protease-independent amoeboid mode of invasion has been described in carcinoma cells and more recently in sarcoma cells on treatment with protease inhibitors. To analyze invasive behavior, we compared highly metastatic sarcoma cells with parental nonmetastatic cells. The metastatic cells exhibited a functional up-regulation of Rho/ROCK signaling and, similarly to carcinoma cells, an amoeboid mode of invasion. Using confocal and traction force microscopy, we showed that an up-regulation of Rho/ROCK signaling leads to increased cytoskeletal dynamics, myosin light chain localization, and increased tractions at the leading edge of the cells and that all of these contributed to increased cell invasiveness in a three-dimensional collagen matrix. We conclude that cells of mesenchymal origin can use the amoeboid nonmesenchymal mode of invasion as their primary invading mechanism and show the dependence of ROCK-mediated amoeboid mode of invasion on the increased capacity of cells to generate force. (Mol Cancer Res 2008;6(9):1410−20)

Introduction

The metastatic potential of tumor cells is the most life-threatening aspect of cancer. The process of metastasis is composed of a series of critical steps known as the metastatic cascade (1). The cascade involves the invasion of cells from the primary tumor into the surrounding tissue, intravasation and transport in the blood or lymphatic system, extravasation, and proliferation of tumor cells at the secondary sites. In this report, we focus on the process of cancer cell invasion as a critical step in metastasis. Recent advances in microarray technologies, real-time *in situ* imaging, and the use of *in vitro* three-dimensional invasion model systems have brought a wealth of new insights into the process of invasion (2). Two main modes of tumor cell invasion into the surrounding tissue have been described (3, 4): the first is a mesenchymal mode that depends on extracellular proteolysis and the second is a recently discovered proteolysis-independent amoeboid mode that depends on the activity of the Rho kinase ROCK. In the amoeboid mode, the up-regulation of ROCK has been hypothesized to assist in the generation of sufficient actomyosin forces that would then allow the tumor cells to deform collagen fibers and push through the extracellular matrix (5). However, the amount of actomyosin forces that are generated by amoeboid-invading versus mesenchymal-invading tumor cells has never been investigated and compared. In contrast, the mesenchymal mode is associated with Rac-dependent F-actin−rich protrusions and does not require an up-regulation of ROCK (6). Recently, it has been reported that proteolysis-dependent invasion can convert to an amoeboid invasion mode when the extracellular proteolytic activity is blocked by inhibitors (4). The ability to undergo a transition from mesenchymal to amoeboid modes would endow tumor cells with an efficient escape from protease inhibitor−based cancer treatment. There is a hope that the combined inhibition of extracellular proteases and ROCK could be effective in preventing tumor cell invasion (3).

To analyze the processes responsible for metastatic capability of tumor cells, we used a rat sarcoma model of metastasis composed of two cell lines (7): nonmetastatic fibroblast-like LW13K2 (K2) cells that were isolated from neoplastic, rat embryo fibroblast cells that had spontaneously transformed *in vitro*, and high metastatic A337/311RP (A3) cells that were derived from the K2 cells.

This rat sarcoma model in which two closely related cell populations have greatly different capacities to induce metastases in animals offers specific advantages for studying *in vitro* metastatic transformation (7). In particular, the close genetic relationship of the cell lines provides a "uniform" genetic background. Therefore, the differences in their metastatic

potential are thought to predominantly reflect differences in their protein expression levels and phosphorylation state.

Using this model, we showed here for the first time that highly metastatic mesenchymal sarcoma cells use the Rho/ROCK-dependent amoeboid mode of invasion as their primary invading mechanism. Furthermore, we showed that the up-regulation of Rho/ROCK signaling relates to an increased invasion, increased recruitment of the myosin light chain (MLC) to the leading edge of the cell, and an increased generation of protrusive force.

Results

Highly Metastatic A3 Mesenchymal Sarcoma Cells Do Not Show Any Detectable Gelatinase Activity

To study the changes related to acquisition of invasive potential, we used a sarcoma model of metastasis consisting of parental nonmetastatic K2 cells and highly metastatic A3 cells derived from K2 cells (7). Because sarcoma cells are of mesenchymal origin and are thought to use the mesenchymal mode of invasion that is dependent on extracellular protease activity (8), we analyzed the gelatinase activity of K2 and A3 cells.

Using an in-gel gelatin zymography assay, we found the matrix metalloproteinase (MMP)-2 to be the only detectable gelatinase secreted into the medium by both K2 and A3 cells as judged by control MMP-2–secreting *src*-transformed embryonic fibroblasts (9). Surprisingly, the highly metastatic sarcoma A3 cells secreted only low levels of inactive MMP-2 proform and no active MMP-2 was detected (Fig. 1A). K2 cells secrete significantly higher amount of pro-MMP-2 and also a small amount of active MMP-2. To further extend the results from the in-gel assay, we did FITC-gelatin zymography. In this assay, any effective amount of gelatinase activity either secreted or membrane bound would be detected. Consistently, no gelatinase activity was observed in highly metastatic A3 cells, and only very low gelatinase activity was detected in the nonmetastatic K2 line. The gelatinase activity in K2 cells was sensitive to the broad-spectrum MMP inhibitor GM6001 (Fig. 1B). These observations suggest that A3 mesenchymal sarcoma cells do not invade via a gelatinase-dependent mesenchymal mode.

Protein Microarray Analysis Reveals Up-Regulation of Rho/ROCK Signaling in Highly Metastatic A3 Cells

To search for an alternative mechanism through which A3 cells exert their metastatic potential, we analyzed differences in protein expression between A3 and K2 cells using protein microarray analysis (Kinex). Kinex protein microarray determines the expression and phosphorylation of selected signaling proteins using a panel of approximately 350 pan-specific and 250 phospho-specific antibodies. Of these 600 antibodies, 83 showed significant changes between A3 and K2 cells (Table 1). The most striking result of this analysis was the up-regulation of the Rho/ROCK signaling pathway (10) as estimated by over-expression of ROCK-I and LIMK1. In addition, the negative regulator of Rho/ROCK pathway, PAK1, was down-regulated by more than 7-fold. Furthermore, we found a significant decrease in integrin β_1 phosphorylation. Because protease-independent invasiveness is correlated with a decreased β_1 integrin expression (4), we analyzed the total β_1 integrin expression in K2 and A3 cells. Indeed, β_1 integrin levels were found to be greatly reduced in A3 cells (Fig. 2B).

To further confirm the up-regulation of the Rho/ROCK pathway, we did a Rho activation assay. RhoA-GTP and RhoC-GTP levels were together almost thrice higher in the metastatic A3 line compared with the nonmetastatic K2 line (Fig. 2A). RhoB-GTP levels were below the detection limit. Both RhoA and RhoC have been previously shown to activate ROCK (11, 12). One possible mechanism explaining higher levels of Rho-GTP in A3 cells could be a down-regulation of RhoGDI. Indeed, the protein microarray analysis showed a 5.9-fold increase of the RhoGDI-degrading enzyme caspase-1 (13) in A3 cells (Table 1). In addition, we analyzed the phosphorylation of the prominent ROCK substrate MYPT-1 (14) and found it greatly elevated in A3 cells (Fig. 2B).

These data together suggest that the Rho/ROCK pathway is functionally up-regulated in A3 cells and, together with the absence of gelatinase activity as shown above, point to a ROCK-dependent amoeboid invasion mechanism.

A3 Cells Exhibit Higher Cytoskeleton Dynamics

The Rho/ROCK pathway has been shown to control cytoskeletal dynamics such as the turnover rate of actin stress fibers and focal adhesions (15). The protein microarray analysis revealed up-regulation of cofilin along with signals leading to cofilin phosphorylation (up-regulation of LIMK1 and ROCK-I). This observation points to increased cofilin phosphorylation dynamics and thus increased dynamics of F-actin polymerization and depolymerization. To quantify the differences in cytoskeleton dynamics between nonmetastatic K2 and metastatic A3 cells, we did two assays: nanoscale particle tracking and magnetic tweezers microrheology.

Nanoscale particle tracking analyzes the random walk of unforced, spontaneously diffusing fibronectin-coated beads. In this work, 4.5-μm-diameter carboxylated polystyrene beads coated with human fibronectin were attached to confluent cells. The beads bind to integrins at the cell surface, initiate focal contact formation, and anchor firmly to the actin cytoskeleton. The beads cannot move unless the focal contacts and actin structures to which they are attached rearrange (16). ATP-driven cytoskeletal rearrangements can be quantified by an apparent diffusivity D* of the beads, measured as the squared distance of bead motion during a 1-s time interval. The variable D* was ~2.5 times greater in A3 cells compared with K2 cells (Fig. 3A). These data are consistent with the idea that the higher invasiveness of A3 cells is facilitated by an increased rate of focal adhesion turnover and cytoskeletal remodeling.

The second assay, magnetic tweezers microrheology, measures the displacement of integrin-bound fibronectin-coated magnetic beads in response to lateral step forces between 0.5 and 10 nN (17). This so-called creep response reports the stability of the bonds that connect the beads with the cell. In the case of fibronectin-coated beads, these bonds are formed by connections between the integrins, focal adhesion proteins, and the actin cytoskeleton (18). The A3 cells display a significantly lower stability of the bonds that connect the beads with the cell, as seen by a significantly higher power-law exponent,

suggesting a more fluid-like behavior typical for cells with higher cytoskeleton dynamics (Fig. 3B).

Phospho-MLC Colocalizes with F-Actin at the Leading Edge of A3 Cells

A previous study (7) has shown that F-actin in the K2 cells is arranged into stress fibers, whereas in A3 cells the F-actin is arranged cortically and concentrated in ruffles at the leading edge of the cell, a typical arrangement for metastatic cells with higher cytoskeletal dynamics (19). To gain further insight into the mechanisms that are responsible for the great differences in cytoskeletal dynamics, we characterized the A3 and K2 actomyosin cytoskeleton with respect to ROCK activity and localization of the ROCK substrate MLC. Functional up-regulation of Rho/ROCK signaling results in phosphorylation and activation of MLC, and subsequent enhancement of actomyosin contractility at the leading edge (14). The distribution and colocalization of phospho-MLC (P-MLC) with F-actin were therefore analyzed.

In the metastatic A3 cells, P-MLC was highly colocalized with cortical F-actin in ruffles, whereas in the nonmetastatic K2 cells this colocalization was much less prominent (Fig. 4A). Quantification of randomly acquired images revealed an $86 \pm$ 8% colocalization of P-MLC with large cortical F-actin structures in A3 cells, in comparison with $35 \pm 10\%$ in the K2 cells (Fig. 4B). To get further insight into the P-MLC distribution in migrating cells, we analyzed P-MLC localization with respect to focal contact marker phospho-paxillin in polarized cells (triangular-shaped cells with clearly defined leading and trailing edge). Confocal analysis of A3 and K2 cells revealed that P-MLC was not enriched in focal contacts at substrate level sections. However, in midcellular confocal section of A3 cells, the P-MLC was enriched at the leading edge, at places with high actin polymerization, and at the trailing edge. In contrast, in K2 cells P-MLC was enriched only at the trailing edge (Fig. 4C, compare with tractions distribution—Fig. 7). These results suggest that at least in two-dimensional cell culture conditions, the actomyosin force is not generated near the focal contact sites but rather above the substrate in regions that are involved in cellular extension formation.

A3 Mesenchymal Sarcoma Cells Show ROCK-Dependent Amoeboid Mode of Invasion

Rho/ROCK signaling has been suggested to be required for cell movement in a local environment that physically restricts locomotion (e.g., during metastatic invasion; ref. 3). To
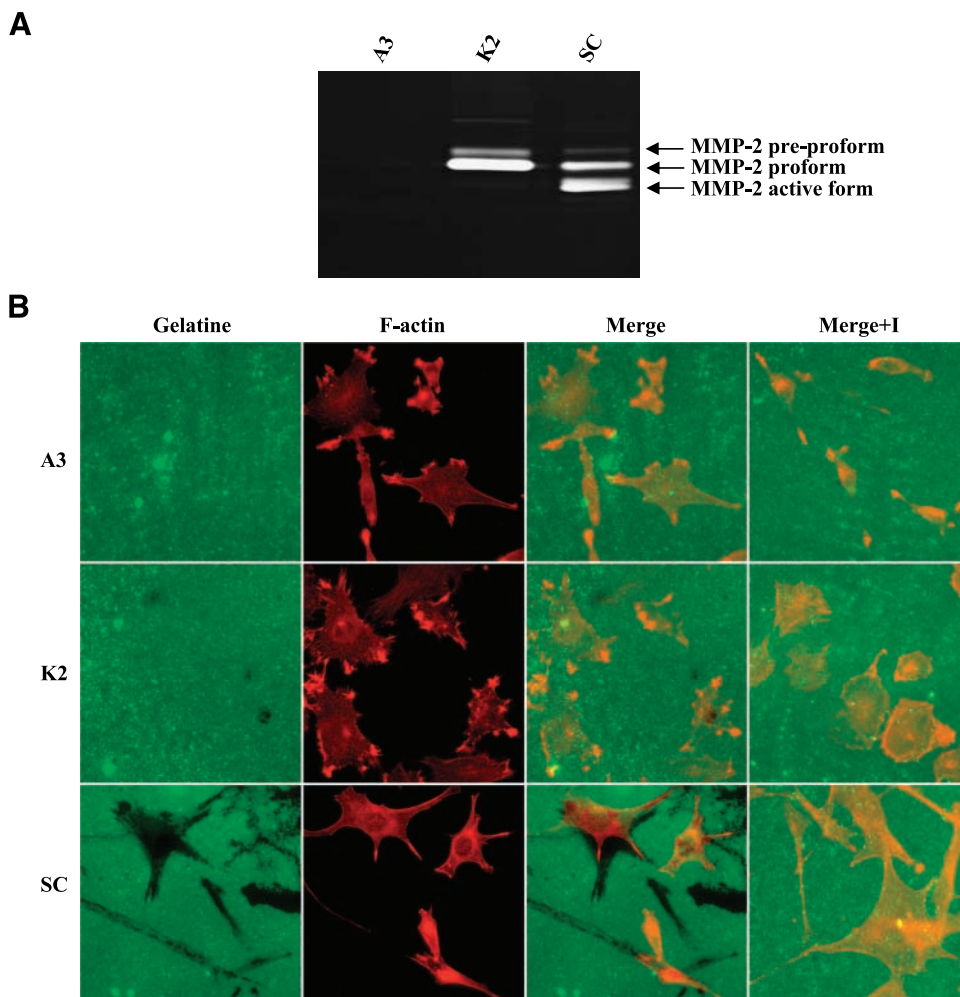
A

B

FIGURE 1. Highly metastatic A3 cells do not show any detectable gelatinase activity. **A.** Gelatin zymography assay of conditioned cell medium. The result is representative of four independent experiments. **B.** FITC-gelatin zymography. Cells were grown on FITC-gelatin–coated (*green*) coverslips for 48 h and then fixed in 4% paraformaldehyde, permeabilized in 0.5% Triton X-100, washed thrice with PBS, blocked in 3% bovine serum albumin, and then stained with Alexa-594-phalloidin (*red*) and examined with epifluorescent microscopy. SC, *src*-transformed embryonic fibroblasts. Scale bar, 20 μm.

Table 1. Protein Microarray Analysis of A3 and K2 Cells

	Fold Change	Protein Name	Antibody	Description
Cytoskeletal dynamics	−7.36	PAK1	Pan-specific	p21-activated serine kinase 1 (α)
	3.43	ROCK-I	Pan-specific	Rho-associated protein kinase 1
	2.86	Rac1/cdc42	Pan-specific	Ras-related C3 botulinum toxin substrate 1
	2.82	PTEN	S370	Phosphatidylinositol-3,4,5-trisphosphate 3-phosphatase. Inhibitory phosphorylation
	2.42	ACK1	Pan-specific	Activated p21cdc42Hs protein-serine kinase
	2.34	Caveolin 2	Pan-specific	Caveolin 2
	−1.96	Catenin b	Pan-specific	Catenin (cadherin-associated protein) β1
	−1.94	Integrin b1	S785	Integrin β1 (CD29). S785 dephosphorylation promotes cell migration.
	1.94	Paxillin	Pan-specific	Paxillin 1
	1.88	Cofilin	Pan-specific	Cofilin 1
	1.84	LIMK1	Pan-specific	LIM domain kinase 1
Cell growth	5.53	MEK5	Pan-specific	MAPK/ERK protein-serine kinase 5 (MKK5)
	3.18	RSK1	Pan-specific	Ribosomal S6 protein-serine kinase 1
	−2.71	RafB	Pan-specific	RafB proto-oncogene–encoded protein-serine kinase
	2.46	MEK3	Pan-specific	MAP kinase protein-serine kinase 3 (MKK3)
	2.24	MEK7	Pan-specific	MAP kinase protein-serine kinase 7 (MKK7)
	2.15	PRKAB1	Pan-specific	5′-AMP–activated protein kinase (AMPK), β-1 regulatory subunit
Cell cycle	3.17	Smad2/3	Pan-specific	SMA- and mothers against decapentaplegic homologue 2/3
	2.7	Jun	Pan-specific	Jun proto-oncogene–encoded AP1 transcription factor
	2.13	p27 Kip1	Pan-specific	p27 cyclin-dependent kinase inhibitor
Apoptosis	5.87	CASP1	Pan-specific	Procaspase-1 (interleukin-1β convertase)
	4.11	CytoC	Pan-specific	Cytochrome C
	2.73	Trail	Pan-specific	Tumor necrosis factor–related apoptosis-inducing ligand
	2.62	RIP2/RICK	Pan-specific	Receptor-interacting serine/threonine-protein kinase 2
Other signaling	−12.17	JNK2	Pan-specific	Jun NH2-terminal protein-serine kinases (stress-activated protein kinase) 2
	3.1	Syk	Pan-specific	Spleen protein-tyrosine kinase
	2.94	STAT1	Pan-specific	Signal transducer and activator of transcription 1
	2.9	CaMK VI	Pan-specific	Serine/threonine-protein kinase DCAMKL1
	2.75	IKKg/NEMO	Pan-specific	I-κ-B kinase γ/NF-κ-B essential modulator
	2.65	STAT5A	Pan-specific	Signal transducer and activator of transcription 5A
	2.54	VEGFR2	Y1054 + Y1059	Vascular endothelial growth factor receptor-tyrosine kinase 2. Activating phosphorylation.
Others	8.41	TyrOH/TH	S19	Tyrosine hydroxylase isoform a. Activating phosphorylation.
	3.64	RONa	Pan-specific	Macrophage-stimulating protein receptor α chain
	2.22	APG2	Pan-specific	Hsp70-related heat shock protein 4

NOTE: Cell lysates of A3 and K2 cells were prepared according to Kinexus company guidelines and the expression (350 antibodies) and phosphorylation (250 antibodies) of selected signaling proteins were tested using Kinex microarrays. Expression or phosphorylation levels in the A3 cells were normalized by the levels in the K2 cells, yielding a ratio for each tested protein. Table 1 is limited to proteins with a fold change of >1.8 or <−1.8. The list presents the average of two experiments.

simulate such an environment of restricted locomotion, we adapted an under-agarose assay that had been used previously to characterize restricted migration of Dictyostelium myosin mutants (20). In the under-agarose assay, A3 cells maintained their overall morphology and assumed an individual mode of migration (Fig. 5A). In contrast, the K2 cells increased their spreading area dramatically and seemed to migrate collectively. F-actin stress fibers became even more abundant and pronounced in K2 cells and were assembled in parallel between neighboring cells, whereas the A3 cells maintained similar F-actin assembly (Fig. 5B) as under the nonrestricted conditions (Fig. 5C). These observations suggest that A3 cells are a priori better adapted to an environment that physically restricts locomotion.

To further test the cell behavior in an environment with physically restricted locomotion, we did the three-dimensional collagen invasion assay (21). The conditions of the assay closely resemble cell movement in a three-dimensional connective tissue environment (3). In agreement with the *in vivo* metastatic capacity of the A3 cells, the *in vitro* three-dimensional collagen invasion assay data revealed a more than 5-fold higher invasiveness of A3 compared with K2 cells (Fig. 6A). These results suggest that the high metastatic potential of A3 cells is a consequence of their increased ability to invade and migrate through connective tissue. Consistent with the under-agarose assay results, the A3 cells in a three-

dimensional collagen matrix exhibited a rounded morphology typical of an amoeboid mode of migration (Fig. 5D). Interestingly, the parental K2 cells also adopted a rounded morphology in three-dimensional collagen, suggesting a dormant albeit less effective potential for amoeboid invasiveness.

To determine whether the amoeboid invasion of A3 cell is ROCK dependent, we analyzed their invasive potential using a high-throughput Matrigel invasion assays in the presence or absence of the ROCK inhibitor Y-27632. Inhibition of ROCK in A3 cells using 10 μmol/L Y-27632 resulted in a 60% decrease in invasion through Matrigel (Fig. 6B) and complete inhibition of invasion into three-dimensional collagen (data not shown). Interestingly, the invasiveness of K2 cells was enhanced in the presence of 10 μmol/L Y-27632 (Fig. 6B). A possible explanation for this enhancement could be the 1.7-fold elevation of MMP-2 activity after ROCK inhibition, as detected by in-gel zymography (data not shown). It could also be due to an increased chemotaxis (data not shown) or a combination of both.

To address the possibility of MMP-dependent invasion, we tested the invasion capacity of both A3 and K2 cells in the presence of a broad-spectrum metalloproteinase inhibitor, GM6001. Neither A3 nor K2 invasiveness was significantly changed by this inhibitor (Fig. 6B). Taken together, these results show that A3 mesenchymal sarcoma cells use the Rho/ROCK-dependent amoeboid mode of invasion.

A3 Cells Generate Higher Forces at the Leading Edge

It has been proposed that an up-regulation of ROCK in cells that undergo an amoeboid mode of invasion increases the actomyosin force generation that in turn enhances the ability to invade and migrate through the extracellular matrix (3); however, data in support of this hypothesis are still lacking. To measure the tractions that K2 and A3 cells exert on their surroundings, cells were plated onto collagen-coated 6.8% acrylamide/0.24% bis-acrylamide gels with a Young's modulus of 13 kPa that corresponds approximately to the stiffness of mammalian soft tissue (22, 23). The cell tractions were computed from the gel deformation measured by the displacement of fluorescent beads with a diameter of 0.5 μm embedded at the gel surface (24). Only polarized cells were used for the analysis. The traction forces at the leading edge in A3 cells were seven times higher compared with K2 cells (Fig. 7A), and the overall traction forces (averaged over the entire cell area) were five times higher in A3 cells (data not shown). Interestingly, in A3 cells the tractions were concentrated at the cell periphery, with prominent localization at the leading edge (Fig. 7B), coinciding with the regions of highest P-MLC concentration. In K2 cells, the tractions were concentrated at the tapered rear end, presumably at sites where long-ranging, tension-carrying stress fibers terminate and connect to the
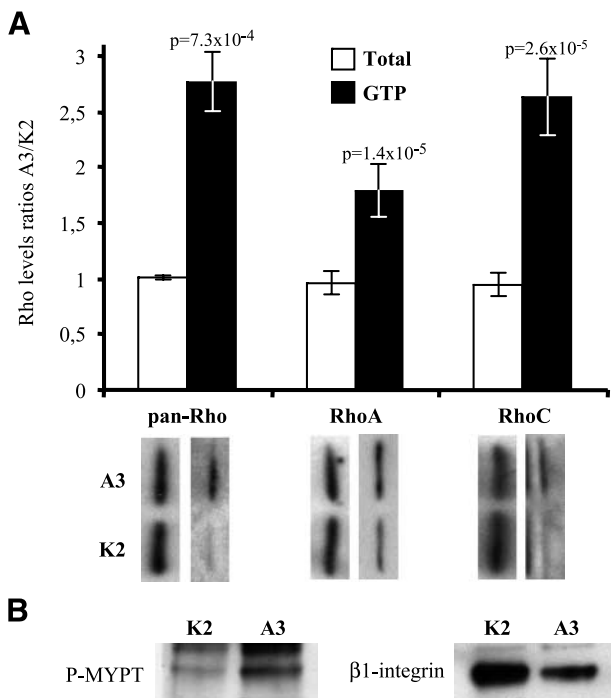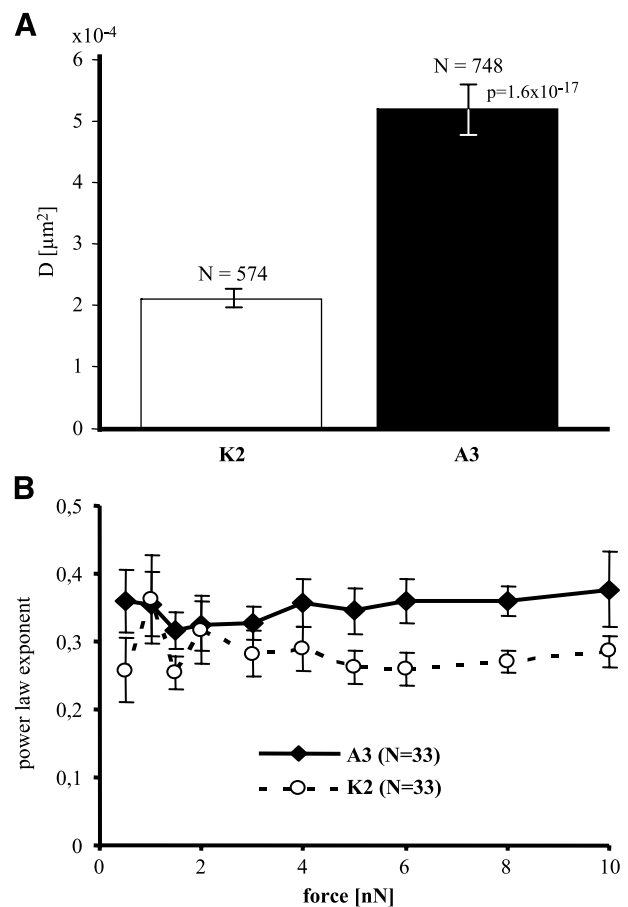

FIGURE 3. Cytoskeleton dynamic. **A.** Nanoscale particle tracking: apparent diffusivity D* of fibronectin-coated beads attached to K2 and A3 cells. D* is a measure of cytoskeletal dynamics and adhesion site turnover. Columns, mean of two experiments; bars, SE. n values represent number of beads tested, and P value was determined from two-tailed t test. **B.** Magnetic tweezers: the bead displacement in response to a staircase-like force followed a superposition of power laws, from which the power law exponent b was determined by a least-squares fit. A3 cells show a higher exponent, suggesting more fluid-like behavior and higher cytoskeletal dynamics. Points, mean of two experiments; bars, SE. n values represent number of beads tested.

FIGURE 2. Up-regulation of Rho/ROCK signaling in highly metastatic A3 cells. **A.** Rho-GTP levels are increased in A3 cells. Cell lysates of K2 and A3 cells were prepared, and total GTP-bound Rho was enriched by absorbing cell lysates to GST-RBD beads and measured by Western blotting using pan-Rho, RhoA, and RhoC antibody. A3/K2 ratio of both total Rho (□) and Rho-GTP (■) was determined. Columns, mean of at least three independent experiments; bars, SD. P values were determined from two-tailed t test. Representative immunoblots of total (*left*) and GTP-loaded (*right*) Rho are shown. **B.** Immunoblot analysis of proteins related to protease-independent invasion in K2 and A3 cells. Antibodies used were anti-phospho-MYPT (Santa Cruz Biotechnology) and anti-β₁ integrin (Cell Signaling Technology).

matrix through focal adhesions that are slow to deadhere. Figuratively, cell movements seem to be driven by a front-wheel drive in A3 cells and impeded by a rear-wheel break in K2 cells. This interpretation of tension-transmitting matrix connections that cycle rapidly in A3 cells but are more stable in K2 cells is consistent with our finding of increased cytoskeletal dynamics in A3 versus K2 cells.

Discussion

In carcinoma cells, the amoeboid cell motility promoted by an up-regulation of ROCK has been shown to correlate with an increased metastatic potential (25, 26). Consistently, other studies have shown that ROCK inhibition reduced the *in vivo* invasive behavior of tumor cells (27, 28), most probably through a reduction in amoeboid tumor cell movement. In this study, we have shown that the high metastatic capacity of A3 cells *in vivo* corresponds to a greatly increased invasiveness in a
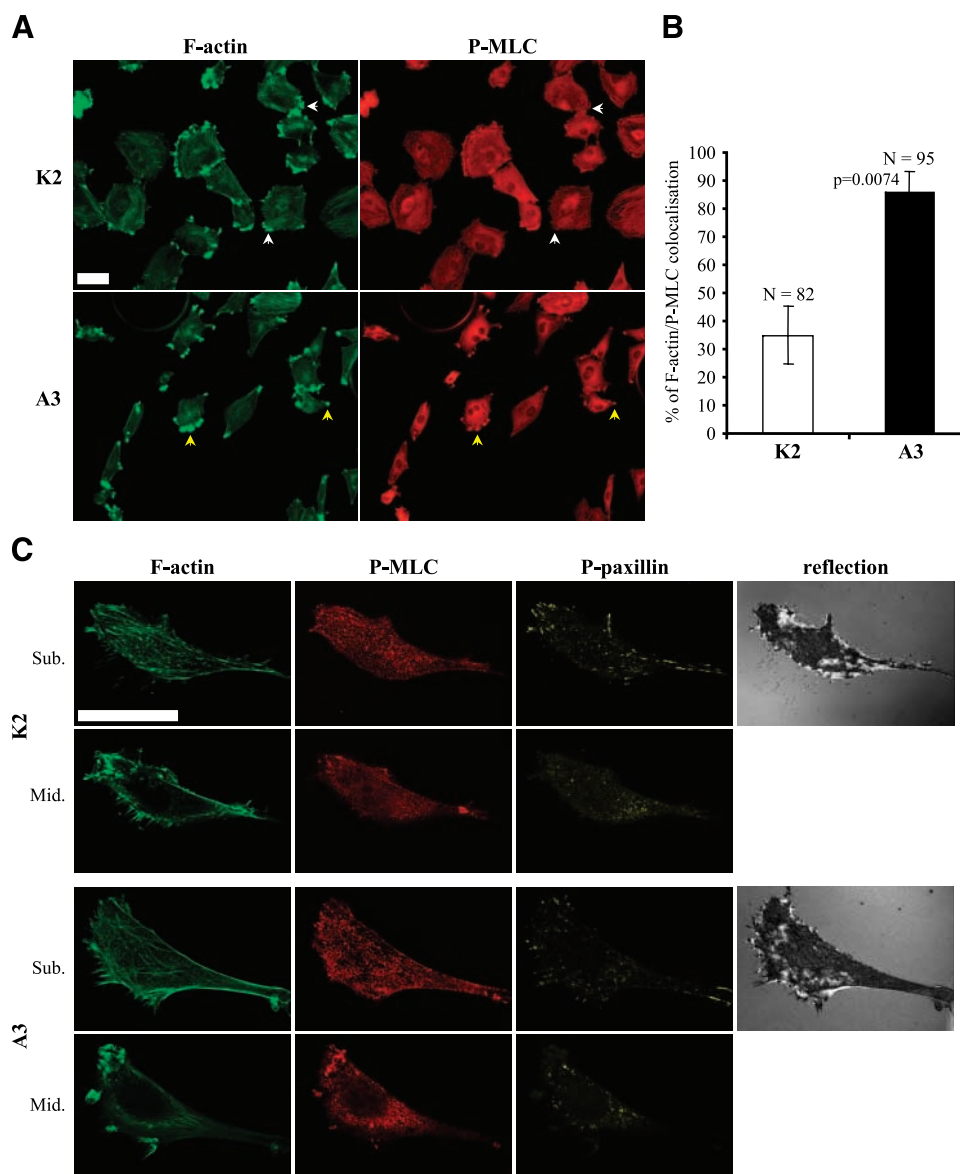
three-dimensional collagen matrix. In addition, we found that the traction forces generated at the leading edge of A3 cells are several fold greater than in their parental nonmetastatic K2 cells.

It has been hypothesized previously that an up-regulation of ROCK in cells that undergo an amoeboid mode of invasion increases actomyosin forces that in turn enhance the ability to invade and migrate through the extracellular matrix (3, 29). Wyckoff et al. (5) reported that the traction forces generated by invading MTLn3E cells are comparable with forces generated by fish keratinocytes. However, an increase of actomyosin force generation in metastatic cells that use an amoeboid mode of invasion in comparison with nonmetastatic control cells has not yet been shown. Our sarcoma model of metastasis based on highly metastatic A3 and nonmetastatic parental K2 cell line offers an ideal approach to this problem. We used traction microscopy to quantify the forces (magnitude, direction, and spatial distribution) that A3 and K2 cells exert on their

extracellular matrix. We found that the traction forces in A3 cells were concentrated at the cell periphery, predominantly at the leading edge coinciding with P-MLC. The preferential localization of traction forces at the leading edge of A3 cells is indicative of forces that facilitate a forward protrusive movement. Taken together, these findings strongly indicate that the functional up-regulation of Rho/ROCK signaling in A3 cells causes an increase in protrusive force generation and therefore an increase in cell invasiveness.

We have shown that A3 cells exhibit an amoeboid morphology in three-dimensional collagen that is characteristic of an amoeboid mode of migration (2-5). However, the non-metastatic K2 cells also adopt rounded, amoeboid-like morphology in three-dimensional collagen. We speculate that the rounded morphology of K2 cells in three-dimensional collagen could be due to a dormant potential of increased Rho activity that is somewhat enhanced by a selective mechanism that leads

FIGURE 4. Enhanced colocalization of large cortical F-actin structures and P-MLC in A3 cells. **A.** Epifluorescent microscopy of K2 and A3 cells visualized with Alexa-594-phalloidin (*green* pseudocolor) and Alexa-488 P-MLC2 antibody (*red* pseudocolor). White arrows, two examples of large cortical F-actin structures in K2 cells without a P-MLC2 colocalization; yellow arrows, two examples of F-actin and P-MLC2 colocalization in A3 cells. **B.** Quantification of colocalization of large cortical F-actin structures and P-MLC2 in K2 and A3 cells. P-MLC2 signal at places of large cortical F-actin structure was considered to be colocalized when the average pixel intensity of the P-MLC2 signal was at least 50% above the average cellular P-MLC2 pixel intensity. Columns, mean of three experiments; bars, SD. *n* values represent number of F-actin structures tested. The *P* value was determined from a two-tailed *t* test. **C.** Confocal sections at substrate (*Sub.*) and midcellular (*Mid.*) levels of polarized K2 and A3 cells visualized with Alexa-488-phalloidin (*green* pseudocolor), Alexa-546 P-MLC2 antibody (*red* pseudocolor), and Alexa-633 phospho-paxillin (*P-paxillin*) antibody (*yellow* pseudocolor). An interference reflection microscopy image is shown for substrate level sections. Scale bars, 25 μm.

to the high invasive phenotype of the A3 cells. To summarize, a rounded morphology of transformed cells invading three-dimensional matrix may not be sufficient for effective amoeboid invasiveness and is therefore not a reliable marker of an effective amoeboid mode of invasion.

Cancer cells can invade three-dimensional matrices by distinct mechanisms, recently defined by their use of extracellular proteases (3, 4). On treatment with protease inhibitors, some tumor cells undergo a mesenchymal to amoeboid transition that allows them to invade in the absence of pericellular proteolysis and matrix degradation (4). Results obtained from studies with

carcinoma cells suggest that cells using an amoeboid invasion mode can generally not switch to a mesenchymal mode. Interestingly, K2 cells seem to exhibit some signs of shift toward the mesenchymal mode on addition of the ROCK inhibitor. The addition of the ROCK inhibitor resulted in increased *in vitro* invasiveness that was accompanied by a 1.7-fold elevation of active MMP-2 secretion (data not shown). Moreover, the closely related *src*-transformed K4 cells, a clonal line derived from the same parental spontaneously transformed rat fibroblasts as K2 cells, exhibit high MMP activity and morphologically resemble cells with a mesenchymal mode of invasion (data not shown).
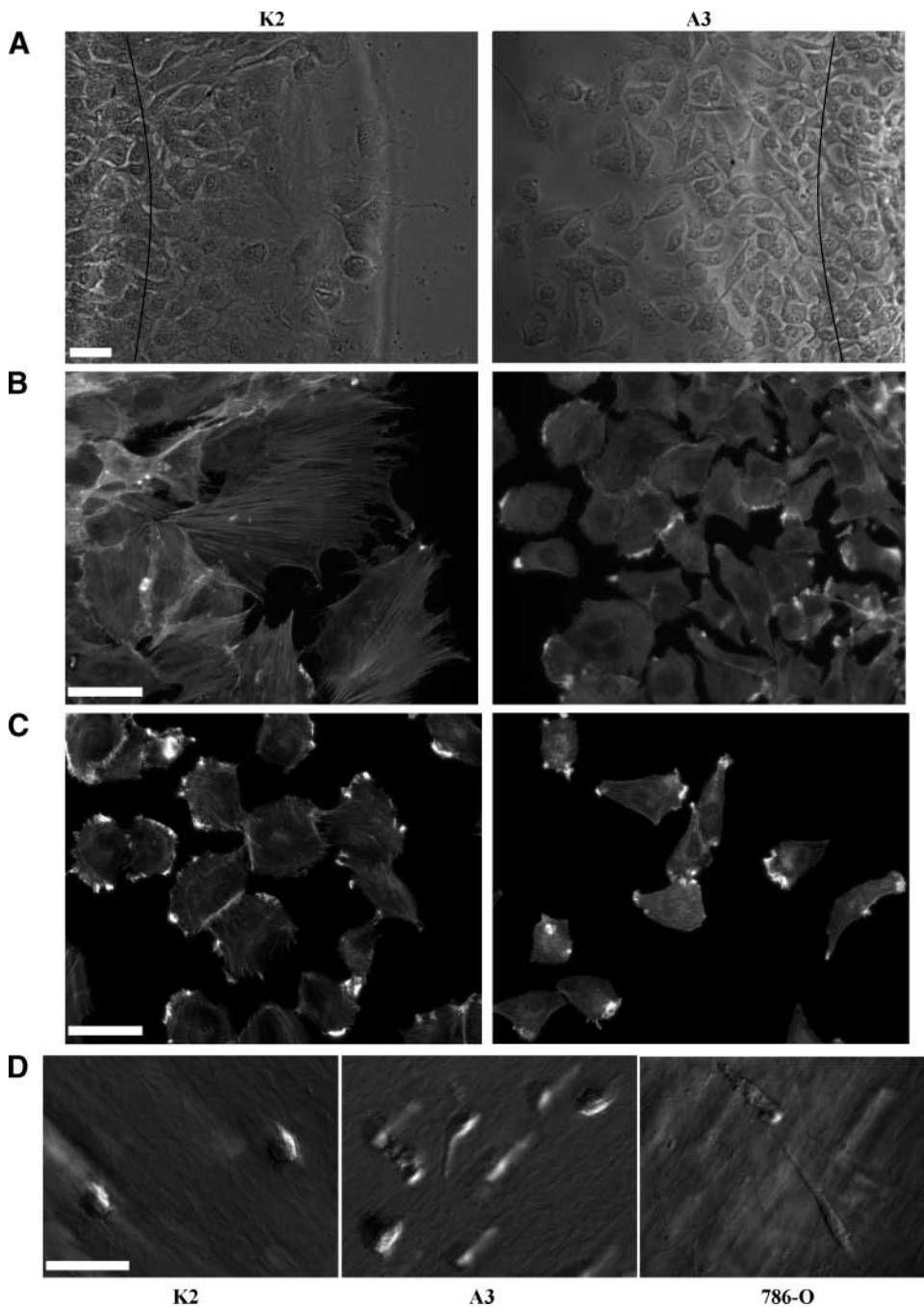

FIGURE 5. A3 cells prefer individual migration with amoeboid-type morphology. **A.** Subconfluent A3 and K2 cells were collected, loaded at a density of 10^4 per well in 0.5% agarose gel, allowed to migrate under the gel for 16 h, and visualized using phase contrast. Black line, boundary between well and agarose. **B.** F-actin stained with Alexa-594-phalloidin in K2 and A3 cells under the same condition as in **A**. **C.** F-actin stained with Alexa-594-phalloidin in A3 and K2 cells that were plated under nonrestricted conditions on glass-bottomed Petri dish. **D.** Amoeboid morphology of K2 and A3 cells invading a three-dimensional collagen matrix (representative modulation contrast image recorded at an invasion depth of 50 μm). Right, mesenchymally invading 786-O kidney cells. Scale bars, 50 μm.
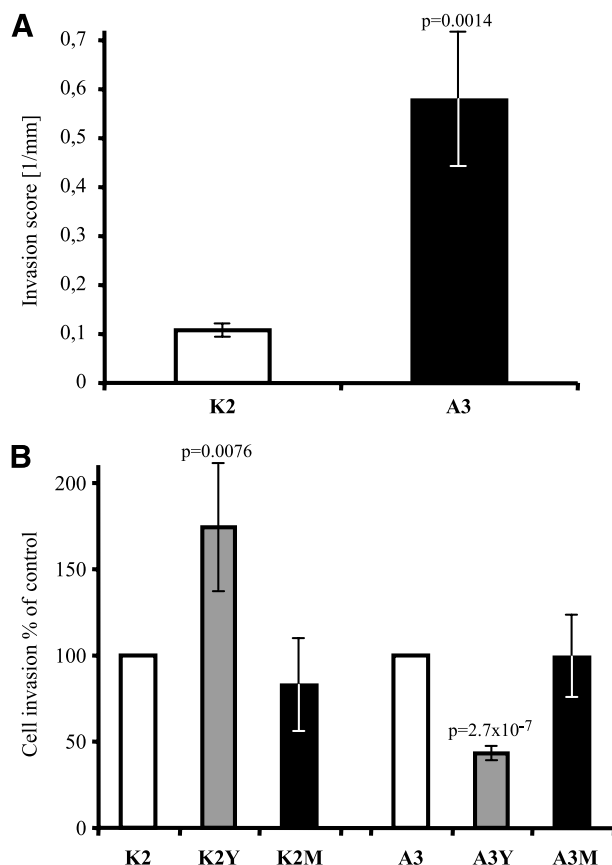
A

B

FIGURE 6. Invasiveness of highly metastatic A3 cells is ROCK dependent. **A.** Three-dimensional collagen invasion. A3 cells (100,000) were seeded on top of a collagen gel. After 3 d of invasion, the number of invaded cells and their invasion depth was determined in 12 randomly selected fields of view. Invasion score was calculated as several invaded cells per mm^2 field of view, multiplied with the average invasion depths. Columns, mean invasion score; bars, SE. *P* value was determined from two-tailed *t* test. **B.** Matrigel invasion assay in the presence of 10 μmol/L of the ROCK inhibitor Y-27632 (*K2Y* and *A3Y*) and 20 μmol/L of the metalloproteinase inhibitor GM6001 (*K2M* and *A3M*). Cell invasion was calculated as percentage of not treated cells and averaged from at least three experiments done in triplicates. Columns, mean; bars, SD. *P* values were determined from two-tailed *t* test and are shown for significant changes in invasiveness.

In this study, we have shown for the first time that highly metastatic mesenchymal sarcoma cells can primarily use the Rho/ROCK-dependent amoeboid mode of invasion. Indeed, previous studies have suggested that Rho/ROCK is involved in controlling the invasion of mesenchymal cells (30-33). We speculate that the metastasis formation of many tumors of mesenchymal origin is promoted by a Rho/ROCK-dependent amoeboid mode of invasion. Determination of the invasion mode that prevails in a particular mesenchymal tumor, together with a more extensive use of Rho/ROCK inhibitors, could significantly improve the effectiveness of mesenchymal tumor treatment in the future.

Materials and Methods
Cultivations and Cell Assays
Cell Culture. K2 cells, full name LW13K2, are spontaneously transformed rat embryonic fibroblasts (34). The A3 cells,

full name A337/311RP, were developed from K2 by neoplastic progression *in vivo* and *in vitro* (7). K2 and A3 cells were maintained in MEM with Hanks' salts supplemented with 10% bovine serum (ZVOS), 0.09% sodium bicarbonate, 0.12 g/L sodium pyruvate, and 1 mmol/L glutamine at 37°C with 5% CO_2.

Collagen Invasion Assays. Collagen R (Serva) and collagen G (Biochrom) were mixed at a ratio of 1:1, and 25 mmol/L sodium bicarbonate and 10 vol% of 10× DMEM were added. The solution was neutralized with 1 mol/L NaOH. Collagen solution (1.2 mL) was placed into each well of a six-well plate, polymerized at 37°C, and incubated with Hank's MEM (H-MEM). After 24 h, 10^5 tumor cells were added and cultured in 2 mL H-MEM. After 3 d, the invasion assay was stopped by fixation with a 2.5% glutaraldehyde solution. The number of invaded tumor cells and their invasion depth was determined in 12 randomly selected fields of view. Invaded cells were imaged using DMI Leica microscope (40×/0.6 HCX Fluotar objective) mounted by CCD camera (ORCA ER, Hamamatsu) and analyzed with Wasabi software.

Matrigel Invasion Assays. Matrigel invasion assays were carried out using Biocoat Matrigel invasion chamber inserts (BD Biosciences) according to the manufacturer's protocol. Briefly, membranes were rehydrated for 2 h in H-MEM and placed in wells containing 10% fetal bovine serum in H-MEM. A total of 10^5 cells suspended in 0.5 mL serum-free H-MEM were added to the top of each chamber (Matrigel coated or control chambers) and then incubated at 37°C in 5% CO_2. After 48 h, the chambers were washed with PBS. Invading cells were fixed in 3.7% formaldehyde for 1 h and stained with 4′,6-diamidino-2-phenylindole. Representative fields were documented by photomicroscopy and the numbers of invading cells were determined from replicate chambers by counting 10 random areas at ×200 magnification.

Under-Agarose Assay. This assay was done as described by Heit and Kubes (35) with the following minor modifications. SeaKem GTG agarose (0.5%) made with 50% H-MEM with 0.25× HBSS and 10% fetal bovine serum was poured into 60-mm glass-bottomed Petri dishes. The agarose was allowed to solidify and wells of 1 mm diameter were cut. Subconfluent A3 and K2 cells were collected, resuspended in serum-free 50% H-MEM with 0.25× HBSS, loaded at a density of 10^4 per well, and allowed to migrate under the gel for 16 h. The cells were visualized either with phase contrast or with Alexa-594-phalloidin staining for F-actin after methanol fixation.

Protein Analysis Techniques
In-Gel Gelatin Zymography. In total, 2×10^5 cells were plated per well of a 24-well plate. After 16 h, cells were washed with PBS and incubated in 300 μL of serum-free medium for 72 h. Aliquots (25 μL) of the conditioned medium were loaded for zymography on a 10% SDS-PAGE gel containing 1 mg/mL gelatin as described (36). Briefly, gel proteins were washed for 1 h in 50 mmol/L Tris-HCl (pH 7.5), 0.1 mol/L NaCl, and 2.5% Triton X-100 and then incubated at 37°C in 50 mmol/L Tris-HCl (pH 7.5), 10 mmol/L $CaCl_2$, and 0.02% sodium azide for 17 h. The gels were stained with Coomassie blue and destained in 7% acetic acid/5% methanol.

Protein Microarrays. Antibody microarray analyses to determine the changes in the expression and phosphorylation state of signaling proteins were done by the Kinex Antibody Microarray service (Kinexus Bioinformatics Corp.).

Microscopy Techniques

FITC-Gelatin Zymography. Coverslips were coated with FITC-gelatin (1 mg/mL), air dried, rehydrated with water for 15 min in 4°C, and fixed with 0.5% glutaraldehyde for 30 min in 4°C. Cells were grown on FITC-gelatin–coated coverslips for 48 h and then fixed in 4% paraformaldehyde, permeabilized in 0.5% Triton X-100, washed thrice with PBS, blocked in 3% bovine serum albumin, and then stained with Alexa-594-phalloidin (Molecular Probes) in blocking solution for 15 min. Coverslips were then washed four times and mounted.

Immunofluorescence Microscopy. Cells were fixed in 4% paraformaldehyde, permeabilized in 0.5% Triton X-100, washed thrice in PBS, and then blocked in 3% bovine serum albumin, incubated with primary antibody for 3 h, washed, and incubated with secondary antibody for 60 min, and then washed again, stained for 15 min with Alexa-594-phalloidin or Alexa-488-phalloidin (Molecular Probes), and mounted. The primary antibodies were mouse P-MLC (Ser[19]) and rabbit phospho-paxillin (Tyr[118]; both from Cell Signaling Technology) and secondary anti-rabbit (Alexa-488 and Alexa-546) and anti-mouse (Alexa-633) antibodies (Molecular Probes). Interference reflection images were visualized using the 488-nm line of an argon laser with no emission filter in front of the detector.

Bright-field and epifluorescent images were captured using a Nikon Eclipse TE2000-S microscope (10×/0.25 and 20×/0.45 Plan Fluor objectives) mounted with VDS Vosskühler CCD-1300 camera and analyzed with Nikon Elements software. Confocal images were acquired by Leica TCS SP2 microscope system using Leica 63×/1.45 oil objective.

Biophysical Techniques

Nanoscale Particle Tracking. Polystyrene beads coated with human fibronectin were attached for 30 min to confluent K2 or A3 cells, and their position was tracked for 5 min from bright-field images recorded with a CCD camera (ORCA ER) at a frame rate of 8.3 Hz. An intensity-weighted center-of-mass algorithm was used to determine the bead positions with 10-nm
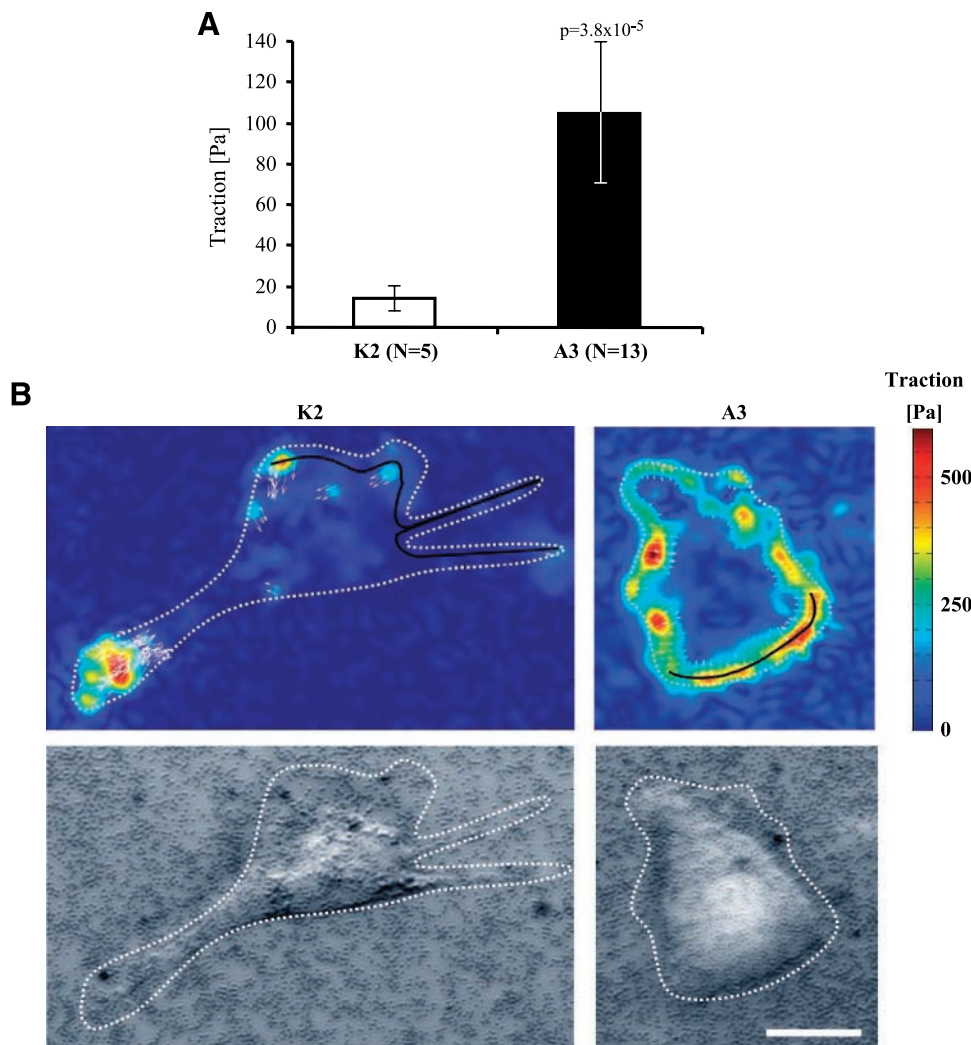

FIGURE 7. Force generation. **A.** Fifty percentile of traction force generated at the leading edge of K2 and A3 cells. Columns, mean; bars, SD. *n* values represent number of cells tested, and *P* value was determined from two-tailed *t* test. **B.** Traction force map of K2 and A3 cells. Black line, leading edge area used for calculation of traction forces. Scale bar, 10 μm.

accuracy (37). An apparent diffusivity D* was calculated as the squared distance a bead had traveled during a 1-s time interval, averaged over all recording times and beads (16, 38).

Magnetic Tweezers. A staircase-like sequence of step forces ranging from 0.5 to 10 nN was applied to superparamagnetic 4.5-μm epoxylated, fibronectin-coated beads (Invitrogen) using magnetic tweezers as described by Mierke et al. (18). Measurements were done after 30 min of bead incubation. Bright-field images were taken at 40 frames per second, and the bead positions were again tracked using an intensity-weighted center-of-mass algorithm. The creep response $J(t)$ of the cells followed a power law in time, $J(t) = a(t/t_0)^b$, where the prefactor a and the power-law exponent b were both force dependent, and the reference time t_0 was set to 1 s. The bead displacement in response to a staircase-like force followed a superposition of power laws (39), from which the power-law exponent b was determined by a least-squares fit.

Traction Force Microscopy. Gels for traction experiments were cast on silane-coated glass slides according to the procedure described by Wang and Pelham (40). Gels with 6.8% acrylamide/0.24% bis-acrylamide were used. The Young's modulus of the gels was measured with a magnetically driven plate rheometer and found to be 13 kPa. Yellow-green fluorescent 0.5-μm carboxylated beads (Molecular Probes) were suspended in the gels and centrifuged at $300 \times g$ toward the gel surface during polymerization at $4°C$. These beads served as markers for gel deformations. The surface of the gel was activated with sulfo-SANPAH (Pierce Biotechnology) and coated with 50 μg/mL bovine collagen G (Biochrom). The cell suspension added to the gel was contained using a silicone ring (In Vitro) attached to the glass slide. Cell tractions were computed from an unconstrained deconvolution (24) of the gel surface displacement field measured before and after cell detachment with an 8 μmol/L cytochalasin D and trypsin/EDTA (0.25/0.02%) in PBS. During measurement, cells were maintained at $37°C$ in humidified atmosphere containing 5% CO_2. Gel deformations were estimated using a Fourier-based difference-with-interpolation image analysis (24, 38).

Disclosure of Potential Conflicts of Interest

Acknowledgments

References

1. Ahmad A, Hart IR. Mechanisms of metastasis. Crit Rev Oncol Hematol 1997; 26:163–73.

2. Sahai E. Mechanisms of cancer cell invasion. Curr Opin Genet Dev 2005;15: 87–96.

3. Sahai E, Marshall CJ. Differing modes of tumour cell invasion have distinct requirements for Rho/ROCK signalling and extracellular proteolysis. Nat Cell Biol 2003;5:711–9.

4. Wolf K, Mazo I, Leung H, et al. Compensation mechanism in tumor cell migration: mesenchymal-amoeboid transition after blocking of pericellular proteolysis. J Cell Biol 2003;160:267–77.

5. Wyckoff JB, Pinner SE, Gschmeissner S, Condeelis JS, Sahai E. ROCK- and myosin-dependent matrix deformation enables protease-independent tumor-cell invasion *in vivo*. Curr Biol 2006;16:1515–23.

6. Vial E, Sahai E, Marshall CJ. ERK-MAPK signaling coordinately regulates activity of Rac1 and RhoA for tumor cell motility. Cancer Cell 2003;4:67–79.

7. Cavanna T, Pokorna E, Vesely P, Gray C, Zicha D. Evidence for protein 4.1B acting as a metastasis suppressor. J Cell Sci 2007;120:606–16.

8. Carragher NO, Walker SM, Scott Carragher LA, et al. Calpain 2 and Src dependence distinguishes mesenchymal and amoeboid modes of tumour cell invasion: a link to integrin function. Oncogene 2006;25:5726–40.

9. Brabek J, Constancio SS, Shin NY, Pozzi A, Weaver AM, Hanks SK. CAS promotes invasiveness of Src-transformed cells. Oncogene 2004;23: 7406–15.

10. Zhao ZS, Manser E. PAK and other Rho-associated kinases—effectors with surprisingly diverse mechanisms of regulation. Biochem J 2005;386: 201–14.

11. Ishizaki T, Maekawa M, Fujisawa K, et al. The small GTP-binding protein Rho binds to and activates a 160 kDa Ser/Thr protein kinase homologous to myotonic dystrophy kinase. EMBO J 1996;15:1885–93.

12. Sahai E, Marshall CJ. ROCK and Dia have opposing effects on adherens junctions downstream of Rho. Nat Cell Biol 2002;4:408–15.

13. Danley DE, Chuang TH, Bokoch GM. Defective Rho GTPase regulation by IL-1β-converting enzyme-mediated cleavage of D4 GDP dissociation inhibitor. J Immunol 1996;157:500–3.

14. Kimura K, Ito M, Amano M, et al. Regulation of myosin phosphatase by Rho and Rho-associated kinase (Rho-kinase). Science 1996;273:245–8.

15. Amano M, Chihara K, Kimura K, et al. Formation of actin stress fibers and focal adhesions enhanced by Rho-kinase. Science 1997;275:1308–11.

16. Bursac P, Lenormand G, Fabry B, et al. Cytoskeletal remodelling and slow dynamics in the living cell. Nat Mater 2005;4:557–61.

17. Alenghat FJ, Fabry B, Tsai KY, Goldmann WH, Ingber DE. Analysis of cell mechanics in single vinculin-deficient cells using a magnetic tweezer. Biochem Biophys Res Commun 2000;277:93–9.

18. Mierke CT, Kollmannsberger P, Zitterbart DP, Smith J, Fabry B, Goldmann WH. Mechano-coupling and regulation of contractility by the vinculin tail domain. Biophys J 2008;94:661–70.

19. Vesely P, Chaloupkova A, Urbanec P, et al. Patterns of *in vitro* behaviour characterizing cells of spontaneously metastasizing K2M rat sarcoma. Folia Biol Praha 1987;33:307–24.

20. Laevsky G, Knecht DA. Cross-linking of actin filaments by myosin II is a major contributor to cortical integrity and cell motility in restrictive environments. J Cell Sci 2003;116:3761–70.

21. Mierke CT, Zitterbart DP, Kollmannsberger P, et al. Breakdown of the endothelial barrier function in tumor cell transmigration. Biophys J 2008;94: 2832–46.

22. Zheng Y, Mak AF. Effective elastic properties for lower limb soft tissues from manual indentation experiment. IEEE Trans Rehabil Eng 1999;7: 257–67.

23. Samani A, Plewes D. An inverse problem solution for measuring the elastic modulus of intact *ex vivo* breast tissue tumours. Phys Med Biol 2007;52: 1247–60.

24. Butler JP, Tolic-Norrelykke IM, Fabry B, Fredberg JJ. Traction fields, moments, and strain energy that cells exert on their surroundings. Am J Physiol Cell Physiol 2002;282:C595–605.

25. Wyckoff JB, Jones JG, Condeelis JS, Segall JE. A critical step in metastasis: *in vivo* analysis of intravasation at the primary tumor. Cancer Res 2000;60: 2504–11.

26. Wang W, Wyckoff JB, Frohlich VC, et al. Single cell behavior in metastatic primary mammary tumors correlated with gene expression patterns revealed by molecular profiling. Cancer Res 2002;62:6278–88.

27. Itoh K, Yoshioka K, Akedo H, Uehata M, Ishizaki T, Narumiya S. An essential part for Rho-associated kinase in the transcellular invasion of tumor cells. Nat Med 1999;5:221–5.

28. Takamura M, Sakamoto M, Genda T, Ichida T, Asakura H, Hirohashi S. Inhibition of intrahepatic metastasis of human hepatocellular carcinoma by Rho-associated protein kinase inhibitor Y-27632. Hepatology 2001; 33:577–81.

29. Mierke CT, Rosel D, Fabry B, Brabek J. Contractile forces in tumor cell migration. Eur J Cell Biol 2008;87:669–76.

30. Fukuda T, Kido A, Kajino K, et al. Cloning of differentially expressed genes in highly and low metastatic rat osteosarcomas by a modified cDNA-AFLP method. Biochem Biophys Res Commun 1999;261:35–40.

31. Banyard J, Anand-Apte B, Symons M, Zetter BR. Motility and invasion are differentially modulated by Rho family GTPases. Oncogene 2000;19:580–91.

32. Nakajima M, Katayama K, Tamechika I, et al. WF-536 inhibits metastatic invasion by enhancing the host cell barrier and inhibiting tumour cell motility. Clin Exp Pharmacol Physiol 2003;30:457–63.

33. Ying H, Biroc SL, Li WW, et al. The Rho kinase inhibitor fasudil inhibits tumor progression in human and rat tumor models. Mol Cancer Ther 2006;5:2158–64.

34. Vesely P, Weiss RA. Cell locomotion and contact inhibition of normal and neoplastic rat cells. Int J Cancer 1973;11:64–76.

35. Heit B, Kubes P. Measuring chemotaxis and chemokinesis: the under-agarose cell migration assay. Sci STKE 2003;2003:L5.

36. Pozzi A, Moberg PE, Miles LA, Wagner S, Soloway P, Gardner HA. Elevated matrix metalloprotease and angiostatin levels in integrin $\alpha 1$ knockout mice cause reduced tumor vascularization. Proc Natl Acad Sci U S A 2000;97:2202–7.

37. Fabry B, Maksym GN, Shore SA, et al. Selected contribution: time course and heterogeneity of contractile responses in cultured human airway smooth muscle cells. J Appl Physiol 2001;91:986–94.

38. Raupach C, Zitterbart DP, Mierke CT, Metzner C, Muller FA, Fabry B. Stress fluctuations and motion of cytoskeletal-bound markers. Phys Rev E Stat Nonlin Soft Matter Phys 2007;76:011918.

39. Hildebrandt J. Comparison of mathematical models for cat lung and viscoelastic balloon derived by Laplace transform methods from pressure-volume data. Bull Math Biophys 1969;31:651–67.

40. Wang YL, Pelham RJ, Jr. Preparation of a flexible, porous polyacrylamide substrate for mechanical studies of cultured cells. Methods Enzymol 1998;298:489–96.